

A normalized thoracic coordinate system for atlas mapping in 3D CT images

Hongkai Wang, Jing Bai ^{*}, Yonghong Zhang

Department of Biomedical Engineering, Tsinghua University, Beijing 100084, China

Received 3 July 2007; received in revised form 23 August 2007; accepted 23 August 2007

Abstract

In this paper, a normalized thoracic coordinate system (NTCS) is defined for rapidly mapping the 4D thoracic organ atlas into individual CT volume images. This coordinate system is defined based on the thoracic skeleton. The coordinate values are normalized by the size of the individual thorax so that this coordinate system is universal to different individuals. For compensating the respiratory motion of the organs, a 4D dynamic torso atlas is introduced. A method for mapping this dynamic atlas into the individual image using the NTCS is also proposed. With this method, the dynamic atlas was mapped into the clinical thoracic CT images and rough positions of the organs were found rapidly. This NTCS-based 4D atlas mapping method may provide a novel way for estimating the thoracic organ positions in low-resolution molecular imaging modalities, as well as in modern 4D medical images.

© 2007 National Natural Science Foundation of China and Chinese Academy of Sciences. Published by Elsevier Limited and Science in China Press. All rights reserved.

Keywords: Atlas mapping; Registration; Segmentation; Molecular imaging

1. Introduction

Anatomical structure information is useful for many applications in molecular imaging. For example, in the case of bioluminescence tomography (BLT), the position and the shape of the major organs are used to reduce the imaging problem to an inverse source problem [1]. Generally, the estimation of the organ position and the organ shape is achieved by registering an anatomical atlas into the individual image. However, registration is always computationally expensive. One idea of solving this problem is to map the atlas into the individual image using a body-based coordinate system. The body-based coordinate system is defined according to the anatomical features and it gives a universal anatomical description to the population. Using the body-based coordinate system, atlas mapping is simplified as the transformation of voxel coordinates,

hence, it is much faster than conventional registration algorithms.

There are many kinds of body-based coordinate systems. The Talairach space [2] and the MNI space [3] are two successful brain-based coordinate systems. Some local organ coordinate systems are also developed, such as the “consistent cardiovascular system of rectangular and spherical coordinates” [4], the “spine-based coordinate system” [5], the “local coordinate system (LCS) for the femoral and tibial cartilage boundaries” [6], and the “thoracic cage coordinate system for recording pathologies locations in lung CT volume data” [7]. However, none of these coordinate systems can define the entire thorax.

There are some difficulties for defining a thoracic coordinate system. The first difficulty is due to the different thoracic sizes among the population. Another difficulty is that the thoracic organs are moving during respiration. Considering these difficulties, a normalized thoracic coordinate system (NTCS) is defined in this paper. In this coordinate system, the coordinate values are normalized by the indi-

^{*} Corresponding author. Tel.: +86 10 62786480; fax: +86 10 62780650.
E-mail address: deabj@tsinghua.edu.cn (J. Bai).

vidual thoracic size so that it is universal to the population. As for solving the problem of organ motion, the 4D NURBS-based cardiac-thorax (NCAT) phantom [8–11] developed at University of North Carolina is used as a dynamic atlas, which can adjust the organ positions according to the respiration phase.

2. Methodology

This section is comprised of two parts: the definition of the NTCS and the method for mapping the dynamic atlas into individual image using the NTCS.

2.1. Definition of the NTCS

2.1.1. Definition of the origin and the z-axis

In order to define a body-based coordinate system, some anatomical landmarks should be selected from the human body. In the Talairach space, the anterior and posterior commissures (AC and PC) are selected as key landmarks [12]. However, in thoracic region, the organs and the ribs move during respiration. So, landmarks should not be selected from these structures. Only the spine is stationary during respiration. Therefore we can select the landmarks from the thoracic vertebrae.

Two landmarks (A and O) are selected at the geometrical centers of the 5th and the 10th thoracic vertebrae (T5 and T10), respectively. The reason of choosing T5 and T10 is that they are not adjacent to the cervical vertebrae or the lumbar vertebrae. Therefore, the effect of neck motions or waist motions on T5 and T10 can be neglected. Another reason is that the line passing the center of T5 and T10 is roughly parallel to the longitudinal axis of human body.

The origin of the coordinate space is defined as landmark O . The z -axis is defined as the axis that points from O to A :

$$\mathbf{z} = \frac{\mathbf{OA}}{\|\mathbf{OA}\|} \quad (1)$$

where \mathbf{z} is the base vector of z direction. \mathbf{OA} is the vector pointing from O to A , $\|\mathbf{OA}\|$ denotes the Euclidean distance between landmarks O and A . Fig. 1a is a sagittal CT spine image which demonstrates landmarks A , O , and the z -axis.

2.1.2. Definition of the xoz plane and the y -axis

The xoz plane is defined as the sagittal mid-plane of the human trunk (see Fig. 1b) because this plane is stationary during respiration. Then, the base vector of y direction (\mathbf{y}) is defined as the normal vector of the xoz plane, which points from the left to the right side of the human trunk.

2.1.3. Definition of the x -axis

The base vector of x direction (\mathbf{x}) is defined as the cross product of \mathbf{y} and \mathbf{z} :

$$\mathbf{x} = \mathbf{z} \times \mathbf{y} \quad (2)$$

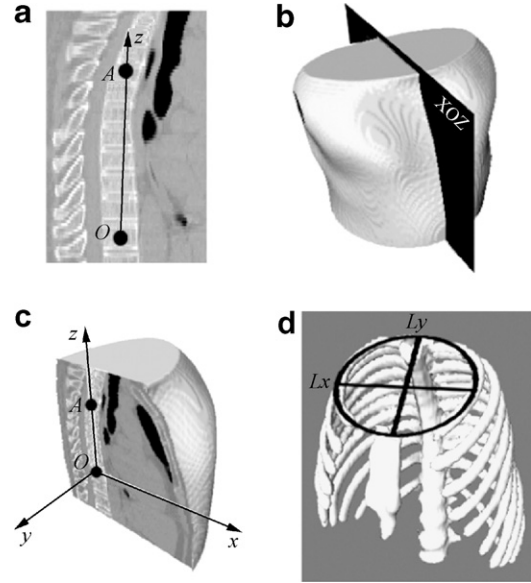


Fig. 1. The definition of the normalized thoracic coordinate system (NTCS). (a) The positions of landmarks A and O ; (b) the xoz plane which is defined as the sagittal mid-plane of human trunk; (c) half of the human trunk cut by the xoz plane; (d) the standard lengths of the NTCS in x and y directions.

Fig. 1c is a picture showing half-part of a human trunk that is cut by the xoz plane, the x -, y -, and z -axes are indicated on it.

2.1.4. Definition of the standard lengths

As derived from above sections, a Cartesian coordinate system of the human thorax can be defined. However, the Cartesian coordinate system cannot give a universal anatomical criterion to different thoracic sizes. It should be normalized to become independent of the thoracic size. The Talairach space is a proportional brain system which is universal to different brain sizes [3]. Learning from the Talairach space, we also make our thoracic coordinate system “proportional”. The key idea is to define three standard lengths (L_x , L_y , and L_z), which represent the thoracic sizes in x , y , z dimensions. Then, the Cartesian coordinate value (x, y, z) is normalized by the standard lengths:

$$\begin{aligned} x' &= x/L_x \\ y' &= y/L_y \\ z' &= z/L_z \end{aligned} \quad (3)$$

where (x', y', z') is the normalized coordinate value, which is independent of the thoracic size. L_z is defined as the Euclidean distance between landmarks O and A , namely $\|\mathbf{OA}\|$, it presents the height of the thorax. The definition of L_x and L_y is more complicated. While breathing, the rib pairs rotate about their costal necks, changing the anterior–posterior diameter of the thorax. Meanwhile, the intercostal muscles also draw up and down the middle part of the rib-body to change the lateral thorax diameter.

Nevertheless, although the diameters of the thorax change distinctly, the diameters of the first and second rib pairs almost keep fixed [13]. Therefore, we can fit an ellipse to the second rib pair, then L_x and L_y are defined as the transverse and lengthwise diameters of the ellipse, respectively (see Fig. 1d).

2.1.5. Definition of the NTCS

As a result of previous definitions, the normalized thoracic coordinate system (NTCS) is defined as the Cartesian coordinate system normalized by the standard lengths (L_x , L_y , and L_z). In order to construct the NTCS in a thoracic volume image, the following key parameters are needed to be determined: landmarks A and O , the xoz plane, x, y, z , L_x , L_y , and L_z .

2.2. Method for atlas mapping using the NTCS

2.2.1. The dynamic atlas

The dynamic atlas which we adopted is the 4D NURBS-based cardiac-thorax (NCAT) phantom developed at the University of North Carolina in Chapel Hill. This is a computerized dynamic thorax phantom for providing a realistic and flexible model of the human anatomy and physiology [8–11]. This phantom can simulate the respiratory motion of the organs. Therefore, it is used to compensate the respiratory motion of the individual organs.

2.2.2. Extraction of the thoracic skeleton

For mapping the NCAT phantom into the individual image, the NTCS should be constructed in both the phantom and the individual image. Since the definition of the NTCS is based on the thoracic skeleton, we need to extract the 3D thoracic skeleton from both the phantom and the individual CT image. The thoracic skeletons of the NCAT phantom and the individual CT image are segmented by single gray-value thresholding.

2.2.3. Construction of the NTCS

A user-interface is developed for constructing the NTCS on the 3D thoracic skeleton. Through the user-interface, two axial slices are manually located to pass the centers of T5 and T10, respectively (see Fig. 2a). Fig. 2b and c shows the two cut images of these axial slices, landmarks A and O are manually located at the centers of the vertebrae in the two cut images, respectively.

After landmarks A and O are located, the symmetric axis passing each of these landmarks are detected in the cut images. Let $l(\varphi)$ be a line rotating about the landmark (A or O) in one of cut images. φ is the angle between $l(\varphi)$ and the row direction of the cut image. $S(\varphi)$ measures the symmetry of the two half-images divided by $l(\varphi)$,

$$S(\varphi) = \sum_{(i \in P) \text{ and } (\bar{i} \in P)} (V(i) - V(\bar{i}))^2 \quad (4)$$

where i is an arbitrary pixel in the cut image, \bar{i} is the symmetrical pixel of i about $l(\varphi)$, P is the set of all the pixels

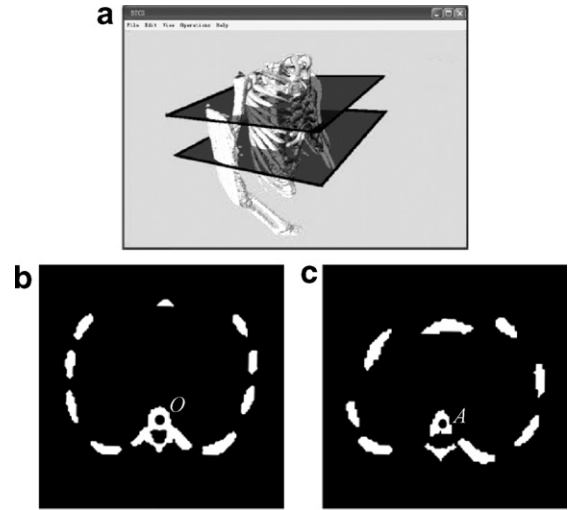


Fig. 2. The selection of landmarks O and A . (a) The user interface demonstrating the selection of the two axial slices that pass the geometrical centers of T5 and T10, respectively; (b) the axial cut image that passes the geometrical centers of T10. Landmark O is located at the geometrical centers of T10; (c) the axial cut image that passes the geometrical centers of T5. Landmark A is located at the geometrical centers of T5.

inside the cut image, $V(i)$ is the pixel value of pixel i . ($i \in P$) and ($\bar{i} \in P$) means both pixel i and \bar{i} are inside the cut image.

According to Eq. (4), the minimum value of $S(\varphi)$ is obtained when $l(\varphi)$ is the symmetric axis of the rib pair. Therefore, the angle of the symmetric axis is

$$\varphi_{\text{opt}} = \arg \min_{\varphi} [S(\varphi)] \quad (5)$$

Fig. 3a and b show the detected symmetric axes in the two cut images. l_A denotes the symmetric axis passing landmark A , l_O denotes the symmetric axis passing landmark O . l_{OA} is the z -axis. l_A , l_O , and l_{OA} roughly form the xoz plane, which is named plane P in Fig. 3c. Therefore, the xoz plane is fitted from l_A , l_O , and l_{OA} using the plane-fitting method

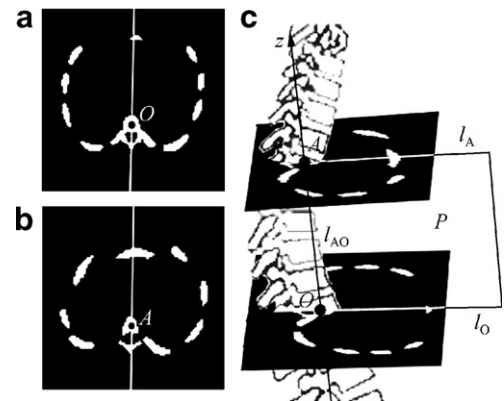


Fig. 3. The detected symmetric axes and the fitted xoz plane. (a) The symmetric axis that passes landmark O ; (b) the symmetric axis that passes landmark A ; (c) the xoz plane is fitted from l_A , l_O , and l_{OA} .

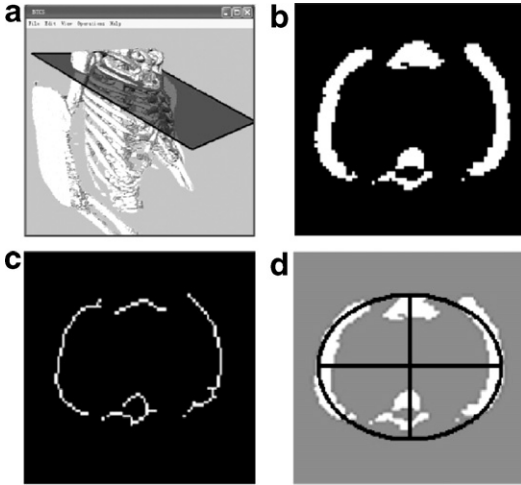


Fig. 4. The calculation of L_x and L_y . (a) The oblique plane which is manually selected to pass the second rib pair; (b) the cut image of the oblique plane in (a); (c) the centerlines of the cut-image in (b); (d) an ellipse is fitted to the centerlines in (c).

proposed by Shen and Shao [7]. Then, x, y, z and L_z are calculated according to positions of landmarks O, A , and the xoz plane.

Through the use-interface, an oblique plane passing the second rib pair is manually located (see Fig. 4a), and a 2D cut image of the second rib pair is also obtained, as shown in Fig. 4b. Morphology thinning is implemented to the cut image to obtain the centerlines of the ribs (see Fig. 4c). Finally, an ellipse is fitted to the centerlines (see Fig. 4d) using the direct least square ellipses fitting method [14]. L_x and L_y are calculated as the transverse and lengthwise diameters of this ellipse.

2.2.4. Dynamic atlas mapping

After the NTCs of the NCAT phantom and the individual image are constructed, the respiration phase of the NCAT phantom is adjusted to coincide with the individual's respiration phase. W. Paul Segars introduced the equations for describing the respiratory motion of the abdominal organs in his NCAT phantom [9]. These equations have a single independent variable t , which represents the respiration phase. The respiratory motions of abdominal organs are simplified as sinusoidal translations of t in three directions (forward, lateral, and vertical directions). Therefore, we simply adjust the value of t to make the respiration phase of the NCAT phantom coincide with the individual's respiration phase. Then, the organ regions in the phantom are mapped into the individual image at the position of the same NTCs coordinate value. Fig. 5 demonstrates the mapping results before and after the adjustment of the respiration phase of the phantom. The highlighted contours in the images are the boundaries of the mapped organ. In Fig. 5a, the individual image is in deep inspiratory phase, while the phantom is set to deep expiratory phase, therefore the mapped lungs are shorter than the individual lungs and the mapped liver is posi-

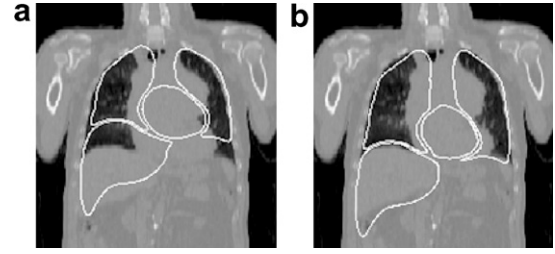


Fig. 5. The adjustment of respiration phase for dynamic atlas mapping. (a) Atlas mapping result with incorrect respiration phase; (b) atlas mapping result after adjustment to correct respiration phase.

tioned upper than the individual liver. In Fig. 5b, the phantom is adjusted to deep inspiratory phase, generating a much more accurate mapping result than Fig. 5a.

3. Experimental results

We chose four organs of the NCAT phantom for mapping, i.e. lung, heart, liver, and spleen. The clinical data sets consisted of 10 normal thoracic CT volumes. The imaging range of these volumes covered from the neck to the upper abdomen. The CT volumes were reconstructed from the clinical CT axial series which were imaged by PHILIPS Brilliance CT 40-slice scanner. The size of every axial slice was 512×512 pixels. Each CT volume contained 120–150 slices. The axial spatial resolution was 0.98 mm and the slice thickness was 3.40 mm.

The proposed method was applied to map the four chosen organs of the phantom into the clinical thoracic CT volumes. The mapping procedure for each individual volume took only a few seconds. In order to compare the computing time of the proposed method with the conventional registration method, a global atlas registration method based on affine transform and mutual information was also performed to the same CT volumes. The registration method spent nearly one minute for each CT volume. The proposed method appeared much faster because it only computes coordinate transformations, while the registration method needs many calculations to optimize the similarity measure (i.e. the mutual information) between the atlas and the individual image.

The mapping accuracy of the proposed method is measured using the overlapping rate between the mapped organ region and the ground truth organ region. The ground truth segmentation is assumed to come from manual labeling of human expert. The overlapping rate is defined as follows:

$$R = \frac{N_{m \cap g}}{N_g} \quad (6)$$

where N_g is the number of the voxels inside the ground truth organ region, $N_{m \cap g}$ is the number of the voxels inside both of the ground truth and the mapped region. The average overlapping rates across the test images is reported in Fig. 6. It is indicated that the average overlapping rates

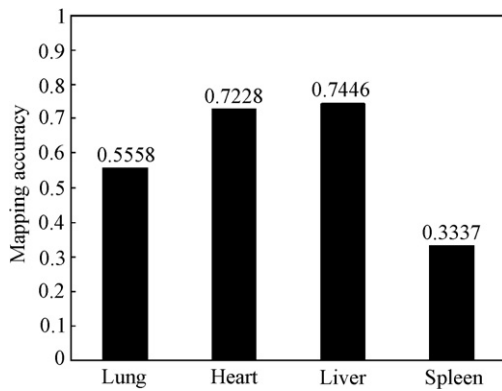


Fig. 6. Mapping accuracy of the NTCS-based atlas mapping algorithm.

of the lung, the heart and the liver are more than 0.5, which means that most parts of these mapped organs overlap with the ground truth area. The overlapping rate of the spleen is relatively small, only 0.3337, which implies that the spleen may not be suitable for atlas mapping, because its position varies too significantly.

For visualization of the mapping results, the mapped surfaces were highlighted inside the individual CT image. Fig. 7 shows six slices of the atlas mapping results, demonstrating in axial, coronal, and sagittal views, respectively. We can see that the reconstructed surfaces roughly align with the edges of the individual organs.

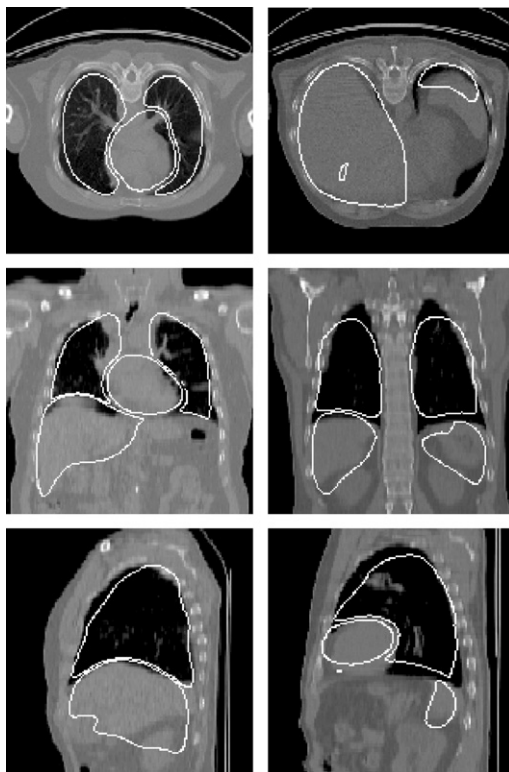


Fig. 7. Slices of the atlas mapping results. The highlighted contours are the surfaces of the mapped organs. The mapping results are demonstrated in axial, coronal, and sagittal views, respectively.

For validation of the intra- and inter-rater variability, two raters were invited to perform atlas mapping for five of the CT volumes. Every rater separately did landmarks locating and respiration phase selection. For each volume, every rater performed twice. The surfaces of the mapped organs were extracted and saved as triangular meshes. Then the intra- and inter-rater variability was measured using the Hausdorff distances between these triangular meshes.

The definition of the Hausdorff distance is described as follows. Let $A = \{a_1, \dots, a_m\}$ and $B = \{b_1, \dots, b_n\}$ denote the vertex sets of two triangular meshes. Then the Hausdorff distance between A and B is defined as

$$H(A, B) = \max(h(A, B), h(B, A)) \quad (7)$$

$$\text{where } h(A, B) = \max_{a \in A} \min_{b \in B} \|a - b\| \quad (8)$$

Hereby $h(A, B)$ is called the directed Hausdorff distance from set A to B . $\|a - b\|$ denotes the Euclidean distance between vertices a and b .

Table 1 reports the indices of the intra-rater variability for the four organs. Each entry of Table 1 reports the averages, minima, maxima, and standard deviations of the Hausdorff distances across the test images. R_1 relates to rater 1, R_2 relates to rater 2.

From Table 1, it can be observed that the maximum Hausdorff distances between intra-rater results is controlled below 21 mm, which is much smaller than the anatomical size of the target organs. It can also be observed that the intra-rater variability of rater 1 is smaller than rater 2, this is because rater 1 practiced more times than rater 2 before the test. Thus we may conclude that more skilled raters produce more stable mapping results.

Table 2 reports the indices of inter-rater variability for the four organs. R_{ij} indicates the mesh generated by rater i at the j th time of atlas mapping ($i = \{1, 2\}, j = \{1, 2\}$). Each entry in the table reports averages, minima, maxima, and standard deviations of the Hausdorff distances between the meshes generated by different raters.

It can be observed from Table 2 that the inter-rater indices between rater 1 and rater 2 are larger than the intra-rater indices of rater 1 (the skilled rater), but close to the intra-rater indices of rater 2 (the unskilled rater). This implies that the inter-rater variability is similar to the intra-rater variability of an unskilled rater. We can also conclude from Table 2 that the inter-rater variability is irrelevant to the target organ, as the indices of the four organs appear similar to each other.

Table 1
Intra-rater variability indices for lung, heart, liver, and spleen (mm)

	R_1	R_2
Lung	4.12, 2.10, 7.37, 2.04	9.44, 6.80, 16.29, 3.89
Heart	3.03, 1.43, 5.78, 1.64	7.05, 6.37, 8.08, 0.71
Liver	4.49, 2.32, 8.03, 2.24	9.88, 5.93, 20.69, 6.18
Spleen	3.66, 1.90, 7.28, 2.36	10.00, 5.82, 16.33, 3.97

Table 2

Inter-rater variability indices for the lungs, the heart, the liver, and the spleen (mm)

	R_{11}	R_{12}
<i>Lung</i>		
R_{21}	8.18, 4.69, 15.44, 4.20	7.72, 5.30, 12.43, 3.11
R_{22}	10.84, 6.39, 16.45, 3.89	10.53, 5.67, 16.42, 4.44
<i>Heart</i>		
R_{21}	7.28, 4.36, 14.10, 3.94	6.74, 3.06, 11.78, 3.63
R_{22}	7.85, 6.00, 11.07, 2.21	7.85, 5.52, 12.67, 2.87
<i>Liver</i>		
R_{21}	8.49, 6.14, 14.64, 3.48	7.73, 5.93, 10.39, 1.80
R_{22}	9.44, 6.89, 16.07, 3.77	9.13, 5.23, 16.07, 4.50
<i>Spleen</i>		
R_{21}	8.54, 4.92, 18.18, 5.62	6.32, 3.08, 12.18, 3.63
R_{22}	10.74, 5.92, 14.76, 3.36	9.19, 3.81, 14.65, 4.35

4. Discussion and conclusion

In this paper, a normalized thoracic coordinate system (NTCS) for atlas mapping in 3D CT image has been defined. The definition is based on the position of the thoracic vertebrae and the sagittal mid-plane of the human trunk. The NTCS is independent of the respiratory movement and it is universal to different thoracic sizes. A method for constructing the NTCS in the 3D CT thorax image is also presented in this paper.

An experiment of atlas mapping has been done to test the feasibility of the NTCS. The 4D NCAT phantom is introduced as a dynamic atlas to be mapped into the clinical thoracic CT images. Results indicate that the NTCS is effective for estimating the rough position of the organs. However, due to the anatomical differences among the population, the same organ of different individuals may vary in size, shape, and location. Simple atlas mapping via the NTCS cannot eliminate these anatomical differences. In order to deal with the anatomical differences and obtain more accurate results, we could use modern medical image segmentation algorithms, like fuzzy-connectedness [15] and deformable models [16]. The NTCS-based atlas mapping provides the initial guess of the organ positions, then these segmentation algorithms start from the initial positions to obtain more accurate results.

One thing should be emphasized is that the purpose of NTCS-based atlas mapping is obtaining the approximate organ positions as quickly as possible, rather than reaching voxel-level mapping accuracy. Modern segmentation algorithms may yield voxel-level or even sub-voxel-level accuracy, but they are more complicated and need much longer time. For those situations in which mapping accuracy is not highly demanded, atlas mapping using the NTCS provides a faster way. For example, in the case of bioluminescence tomography (BLT) of small animals, approximate positions of the major organs are used as prior anatomical information for the reconstruction algorithm. Wang and Cong used a semi-automatic deformation

method to register the animal atlas with the individual micro-CT image and obtained the approximate positions of the major organs [1]. This registration procedure is time consuming and needs many user-interventions. Comparing to the registration-based algorithms, the NTCS is faster and easier for implementation. Using the NTCS, approximate anatomical information can be obtained within seconds, therefore the reconstruction procedure of BLT imaging can be remarkably sped up. Another possible application of the NTCS is in the field of organ segmentation [17–25], in which the NTCS-based atlas mapping could rapidly estimate the rough location and shape of the target organs. This may offer useful initial information to the segmentation algorithms.

As for future work, we may apply the NTCS to estimating the positions of the major organs in the micro-CT images of the small animals. This work may provide useful anatomical structure information for the molecular imaging of small animals, such as bioluminescence tomography (BLT) [1], fluorescent molecular tomography (FMT) [21], and etc. Furthermore, the NTCS-based dynamic atlas mapping method can also be extended to tracing the organ positions in 4D medical images, such as dynamic cardiac images.

Acknowledgements

This work was partially supported by the National Natural Science Foundation of China (Grant No. 60331010), the Tsinghua-Yue-Yuen Medical Science Foundation, the National Basic Research Program of China, the Hi-Tech Research and Development Program of China, and the Special Research Fund for the Doctoral Program of Higher Education of China.

The authors thank Dr. William Paul Segars in Johns Hopkins Outpatient Center and Dr. Benjamin M.W. Tsui at University of North Carolina at Chapel Hill for providing the executable file of the 4D NCAT phantom and giving suggestion of using it. We also appreciate Dr. Jiacheng Liu for providing the clinical thoracic CT images.

References

- [1] Wang G, Cong WX, Durairaj K, et al. In vivo mouse studies with bioluminescence tomography. *Opt Express* 2006;14(17):7801–9.
- [2] Talairach J, Tournoux P. Co-planar stereotaxic atlas of the human brain: 3 dimensional proportional system – an approach to cerebral imaging. New York: Thieme Medical Publishers; 1988.
- [3] Evans AC, Collins DL, Mills SR, et al. 3D statistical neuroanatomical models from 305 MRI volumes. In: *Proceedings of IEEE-nuclear science symposium and medical imaging conference*, 1993.
- [4] Malmivuo JA, Wikswo J, Barry WH, et al. Consistent system of rectangular and spherical coordinates for electrocardiography and magnetocardiography. *Med Biol Eng Comput* 1977;4:413–5.
- [5] Vrtovec T, Likar B, Pernuš F. Spine-based coordinate system. In: *Proceedings of IEEE-engineering in medicine and biology 27th annual conference*, Shanghai; 2005. p. 5120–23.
- [6] Kauffmann C, Gravel P, Godbout B, et al. Computer-aided method for quantification of cartilage thickness and volume changes using

- MRI: validation study using a synthetic model. *IEEE Trans Biomed Eng* 2003;50(8):978–88.
- [7] Shen H, Shao M. A thoracic cage coordinate system for recording pathologies in lung CT volume data. In: *Proceedings of IEEE-nuclear science symposium conference*, Portland; 2003. p. 19–25.
- [8] Segars WP, Lalush DS, Tsui BMW. A realistic spline-based dynamic heart phantom. *IEEE Trans Nucl Sci* 1999;46(3):503–6.
- [9] Segars WP, Lalush DS, Tsui BMW. Modeling respiratory mechanics in the MCAT and spline-based MCAT phantoms. *IEEE Trans Nucl Sci* 2001;48(1):89–97.
- [10] Segars WP, Tsui BMW. Study of the efficacy of respiratory gating in myocardial SPECT using the new 4-D NCAT phantom. *IEEE Trans Nucl Sci* 2002;49(3):675–9.
- [11] Tsui BMW, Segars WP, Lalush DS. Effects of upward creep and respiratory motion in myocardial SPECT. *IEEE Trans Nucl Sci* 2000;47(3):1192–5.
- [12] Han Y, Park HW. Automatic brain MR image registration based on Talairach reference system. In: *Proceedings of IEEE-international conference on image processing*. Barcelona; 2003. p. 14–17.
- [13] Marieb EN. *Human anatomy and physiology*, 4th ed., vol. 4. California: Benjamin/Cummings Science Publishing; 1998.
- [14] Fitzgibbon A, Pilu M, Fisher RB. Direct least square fitting of ellipses. *IEEE Trans Pattern Anal Mach Intell* 1999;21(5):476–80.
- [15] Zhou YX, Bai J. An atlas-based fuzzy connectedness method for automatic tissue classification in brain MRI. *Prog Nat Sci* 2006;16(10):1106–10.
- [16] Svoboda D, Matula P. Tissue reconstruction based on deformation of dual simplex meshes. *Discrete Geometry Comput Imagery* 2003;2886:514–23.
- [17] Park H, Bland PH, Meyer CR. Construction of an abdominal probabilistic atlas and its application in segmentation. *IEEE Trans Med Imag* 2003;22(4):483–92.
- [18] Rohlfing T, Russakoff DB, Maurer CR. Performance-based classifier combination in atlas-based image segmentation using expectation-maximization parameter estimation. *IEEE Trans Med Imag* 2004;23(8):983–94.
- [19] Rohlfing T, Maurer CR. Multi-classifier framework for atlas-based image segmentation. *Pattern Recognit Lett* 2005;26(13):2070–9.
- [20] Kikinis R, Shenton ME, Iosifescu DV, et al. A digital brain atlas for surgical planning, model-driven segmentation, and teaching. *IEEE Trans Visual Comput Graph* 1996;2(3):232–41.
- [21] Lorenzo-Valdes M, Sanchez-Ortiz GI, Elkington AG, et al. Segmentation of 4D cardiac MR images using a probabilistic atlas and the EM algorithm. *Med Image Anal* 2004;8(3):255–65.
- [22] Ehrhardt J, Handels H, Malina T, et al. Atlas-based segmentation of bone structures to support the virtual planning of hip operations. *Int J Med Inform* 2001;64(2-3):439–47.
- [23] Qatarnah SM, Noz ME, Hyodynmaa S, et al. Evaluation of a segmentation procedure to delineate organs for use in construction of a radiation therapy planning atlas. *Int J Med Inform* 2003;69(1):39–55.
- [24] Bosc M, Heitz F, Armspach JP. Statistical atlas-based sub-voxel segmentation of 3D brain MRI. In: *Proceedings of IEEE-international conference on image processing*. Barcelona; 2003. p. 1777–80.
- [25] Zhou Y, Bai J. Organ segmentation using atlas registration and fuzzy connectedness. In: *Proceedings of the 27th annual international conference IEEE-EMBS*, Shanghai, China; 2005. p. 3241–44.